DOI: 10.1002/adma.((please add manuscript number))

Article type: Communication

High Operating Temperature Direct Ink Writing Of Mesoscale Eutectic Architectures

J. William Boley, Kundan Chaudhary, Thomas J. Ober, Mohammadreza Khorasaninejad, Wei-Ting Chen, Erik Hanson, Ashish Kulkarni, Jaewon Oh, Jinwoo Kim, Larry K. Aagesen, Alexander Y. Zhu, Federico Capasso, Katsuyo Thornton, Paul V. Braun, and Jennifer A. Lewis*

Dr. J. W. Boley, K. Chaudhary, Dr. T. J. Ober, Prof. J. A. Lewis

John A. Paulson School of Engineering and Applied Sciences

Wyss Institute for Biologically Inspired Engineering

Harvard University

Cambridge MA 02138, USA

Email: jalewis@seas.harvard.edu

Dr. M. Khorasaninejad, Dr. W.T. Chen, A. Y. Zhu, Prof. F. Capasso

John A. Paulson School of Engineering and Applied Sciences

Harvard University

Cambridge MA 02138, USA

J. Oh

University of Waterloo

Waterloo ON N2L 3G1, Canada

E. Hanson, Dr. L. K. Aagesen Prof. K. Thornton

This is the author manuscript accepted for publication and has undergone full peer review but has not been through the copyediting, typesetting, pagination and proofreading process, which may lead to differences between this version and the <u>Version of Record</u>. Please cite this article as <u>doi:</u> 10.1002/adma.201604778.



Department of Materials Science and Engineering

University of Michigan

Ann Arbor, MI 48109, USA

A. Kulkarni, J. Kim, Prof. P. V. Braun

Department of Materials Science and Engineering

Frederick Seitz Materials Research Laboratory

University of Illinois at Urbana-Champaign

Urbana, IL 61801, USA

Keywords: 3D printing, eutectics, self-assembly, metamaterials, structural color

Author Ma



The ability to rapidly fabricate materials with controlled periodicity on length scales near the wavelength of visible light is important for optical devices,^[1, 2] cloaking,^[3-6] beam shaping,^[7-1] and other applications. Most optical materials are fabricated using lithographic techniques^[12] that provide exquisite control over their composition and feature size. Recently, directional solidification of eutectic materials has been investigated as an alternate approach for fabricating optical devices. Upon cooling from the molten state, these materials self organize into lamellar, rod-like, or other periodic motifs.^[13] Remarkably, these structures often bear a striking resemblance to lithographically fabricated photonics^[14-16] and metamaterials,^[17, 18] and, in some cases, exhibit unique structures that give rise to a localized surface plasmon resonance.^[19, 20] However, despite their promise, scant attention has been given to simultaneously patterning and directionally solidifying eutectic materials.

Here, we report a new process for creating mesoscale eutectic architectures, known as high operating temperature direct ink writing (HOT-DIW). Unlike micro-pull down methods that control directional solidification, [19,20] HOT-DIW also enables direct patterning of eutectic materials. Specifically, we print a molten eutectic ink composed of a silver chloride (AgCl)-potassium chloride (KCl) onto a glass substrate in air under ambient conditions. The ink solidifies when cooled below its eutectic temperature ($T_E \approx 319^{\circ}\text{C}$). [21-23] By controlling the printing temperature and speed, we create mesoscale eutectic AgCl-KCl architectures composed of lamellar features oriented along the printing direction, whose periodic spacing can be systematically varied between ~100 nm and 2 μ m. Heat transfer calculations and phase field modeling are carried out to understand the influence of key printing parameters on their directional solidification. Given their periodicity, these mesoscale eutectic architectures serve as diffraction gratings that manipulate light in the visible and infrared regimes. By selectively



etching KCl lamellae followed by coating silver onto the remaining AgCl lamellae, their optical reflectivity is enhanced by an order of magnitude. While we focused on the AgCl-KCl system due to its relatively low eutectic temperature, lamellar microstructure, and ability to print in air,^[14] HOT-DIW enables patterning of nearly any material whose melting point is below 700°C, the current maximum hot operating temperature, including polymers, glasses, and metal eutectics (**Figure S1**).

The HOT-DIW platform consists of a custom-designed graphite nozzle that is locally heated to 400°C (i.e., $T_{nozzle} > T_E$) through which the molten AgCl-KCl ink flows (**Figure 1a**). This molten ink consists of a low viscosity (~ 2-3 mPa·s), Newtonian fluid that undergoes directional solidification upon contact with the cold substrate (held at room temperature). For printing speeds of interest (< 1 mm·s·1), surface forces play a significant role due to the low capillary number ($C_a \le 1.2 \times 10^{-4}$) (see Methods). To produce uniform printed filaments, the applied pressure must not exceed the Laplace pressure at the nozzle-substrate interface, which necessitates a small gap height (~10 µm) between the nozzle and the substrate during printing (**Figure 1b**, **Movie 1**). The solidification front trails the hot nozzle, as the nozzle is translated across the substrate at a printing speed, v. Upon solidification of the eutectic ink, the AgCl and KCl phases self-organize into a lamellar architecture (**Figure 1c**) with a characteristic spacing, L, which is governed by the rates of solidification and diffusion ahead of the solidification front L^{122} and whose relative lamellar widths are determined by the eutectic composition (i.e., 62% AgCl and 38% KCl by volume).

To demonstrate HOT-DIW, we produced meander line patterns composed of eutectic AgCl-KCl filaments that are nominally 2 mm wide, corresponding to the outer diameter of the nozzle used. The representative eutectic filaments shown in **Figure 2a** are printed at a speed of 0.18 mm s⁻¹. Their curved top surface arises due to surface area minimization of the molten



eutectic ink (surface tension, $\sigma \approx 146 \text{ mN} \cdot \text{m}^{-1})^{[25]}$ prior to solidification, while their flat bottom surface conforms to the underlying substrate. The lamellar features observed on the top and bottom surfaces exhibit long-range order, persisting along the length and through the thickness of the printed filaments (**Figure 2b**, **Figure S2**). The lamellar spacing (and orientation) measured at the two edges and center region of these filaments are $668 \pm 84 \text{ nm}$ ($70 \pm 7^{\circ}$) and $324 \pm 32 \text{ nm}$ ($3 \pm 4^{\circ}$), respectively, where the printing direction is defined as 0° . These values are in good agreement with predicted values of 716 nm and 67° (edge) and 309 nm and 0° (center) determined by phase-field modeling.

The lamellar spacing within the printed eutectic architectures can be systematically controlled by varying the printing speed (**Figure 3**). At low speeds ($v \le v_{crit}$), the printed eutectic filaments exhibit a periodic lamellar architecture, whose characteristic spacing decreases with increasing v (Figure 3a). However, when $v > v_{crit}$, multiple lamellar domains are observed that progress inward from each edge ultimately impinging in the center of the filament (Figure 3a). A transition from a uniform to non-uniform lamellar architecture occurs at v_{crit} ($\approx 1 \,\mathrm{mm\cdot s^{-1}}$). To better understand these experimental observations, two-dimensional (2D) heat transfer calculations are carried out to determine the influence of printing speed, v, on the shape and evolution of the solidification front within the printed filaments (Figure 3b, **Figure S3a**). When $v \le v_{crit}$, the temperature field remains constant throughout the thickness of the filament resulting in a vertical solidification front that gives rise to a uniform lamellar architecture (Figures 3b). At v_{crit} , the Péclet number, P_e , is close to unity ($P_e \approx 0.85$) (see Methods). When $v \leq v_{crit}$, the speed of the solidification front is approximately identical to v. However, this relationship falls off sharply when $v > v_{crit}$ and the temperature field becomes non-uniform throughout the thickness of the filament shifting the solidification front away from the nozzle to the filament edges (Figure 3b). Under these conditions, the solidification



front deviates from a vertical orientation (**Figure 3b**), as the advective heat transfer rate associated with a given printing speed becomes large relative to thermal diffusion through the filament thickness ($P_e > 0.85$). The HOT nozzle moves away from the deposited eutectic ink quickly enough such that its influence on the solidification front lessens as v increases (**Figure S3a**). This weaker dependence of the solidification front speed on v translates to a weaker dependence of L on $v^{[22]}$ (**Figure 3c**). Therefore, above $v_{crit} \approx 1 \text{ mm·s·}^{-1}$, the direction of solidification and, hence, lamellar growth changes from predominately parallel to the print path to primarily inward from each filament edge, while remaining vertical to the substrate. As these lamellar features converge at the filament center, domain boundaries arise leading to a non-uniform architecture (**Figure 3a**). Based on simulations, the printed filaments begin to solidify roughly 200 µm downstream from the HOT nozzle-molten ink interface (**Figure 3b**).

The lamellar spacing L within the printed eutectic features can be varied from 2.3 μ m down to 140 nm as the printing speed, v, is increased up to v_{crit} . These periodic features lie within the range of values required for manipulating light in the visible and infrared regimes. We note that the HOT nozzle imposes a curvilinear high temperature boundary (**Figure S3b**) that leads to a gradient in lamellar spacing from the filament edge to its center. We also find that all values of L observed for printed architectures fabricated at $v \le v_{crit}$ can be collapsed onto a single curve (**Figure 3d**) that corresponds to the solidification front velocity ($V = v \sin \varphi$). Eutectic materials that form lamellar microstructures when solidified with minimum undercooling should exhibit a theoretical spacing L, defined by the power law $L = cV^{-0.5}$, where the constant of proportionality, c, is dependent on the material properties of the system. By fitting our data to this model, we find good agreement with the predicted power law dependence and obtain a value of $c = 5.40 \times 10^{-9} \pm 0.13 \times 10^{-9}$.



The periodic architecture coupled with the precise control over the lamellar spacing achieved in printed filaments fabricated at $v \leq v_{crit}$ make them effective diffraction gratings (Figure 4a). The angle-dependent spectra measured from light diffracted from the bottom surface of the filaments follow the same trend as simulations for a model grating (**Figure 4b**). By varying v (and therefore L), we can tailor the incident angle θ where the central wavelength of the visible spectrum ($\lambda = 515 \text{ nm}$) is reflected (**Figure 4c**). The measured and simulated normalized diffraction efficiency (defined as the corresponding reflected signal normalized by the respective maximum reflected over the plotted region) show that the spectrum shifts to larger θ for increased v (decreased L). Further comparison between these experimental results and model predictions can be made by estimating L from the first order diffraction response, where $L = \lambda_{max}/\sin\theta_{fo}$ and λ_{max} is the wavelength at which the normalized diffraction efficiency is maximized for each angle in the first order diffraction, θ_{fo} (**Figure S4**). The primary peaks observed experimentally are accompanied by pronounced shoulder peaks that likely arise due to the waviness of the lamellae within the printed filaments (Figure S5). Light transmitted through the bottom surface of the printed filament would be affected by the wavy interfaces between the two phases, since they each transmit light in the visible range. The measured and simulated absolute efficiencies of the as-printed samples are low (less than 3% in all cases) and follow similar trends (Figures S6 a and b). The modest difference in absolute efficiencies may stem from variations in the lamellar spacing within printed filaments that are not well captured by the simulations. In all cases, their measured angular response is in good agreement with the predicted response (Figures 4b-c). In addition, the estimated values of L from the measured spectra are consistent with those observed directly by scanning electron microscopy (Figure **S4**). Notably, we also find that the printed architectures exhibit vivid structural color, which can be tuned by controlling the printing speed (**Figure S7**, **Movies 2-3**).



To further improve the diffraction grating performance, we selectively etched the KCl phase from printed eutectic filaments ($v = 0.05 \,\mathrm{mm}\cdot\mathrm{s}^{-1}$, $L = 801 \,\mathrm{nm}$). These features are selected to maximize the applicable range of wavelengths and the amount of light diffracted in the first order. The as-printed eutectic filaments exhibit a low diffraction efficiency (< 1.6%) (Figure 4d). Upon removing the KCl phase, the diffraction efficiency increased to ~2.5% due to the increase in refractive index contrast between the resulting air voids and adjacent AgCl lamellae. By depositing a silver coating (450 nm thick) onto the AgCl lamellae, we observed an order of magnitude increase in diffraction efficiency (~15%) compared to the as-printed gratings. The observed enhancement is in good agreement with their simulated absolute efficiencies (Figure S6c).

In summary, we introduce a new printing method, HOT-DIW, for patterning eutectic materials for optical applications in the visible and IR regimes. By controlling the print speed, the lamellar spacing within the printed filaments can be systematically varied between approximately $100\,$ nm to $2\,$ μm . Both the as-printed mesoscale architectures and the metallo-dielectric variants templated from those structures may find application as Bragg reflectors. Upon further optimization, this method should allow the programmable patterning of a wide range of materials, including polymers, metal eutectics, and glass, in both large area and multilayer formats.



Methods

Materials Systems: The eutectic AgCl-KCl ink is prepared by mixing as-received AgCl (99.997%, Alfa Aesar) and KCl (99%, Sigma-Aldrich) powders in a glass petri dish on a mass balance (Mettler AE 50) at 82 and 18 wt.% (70 and 30 at.%), respectively, corresponding to its eutectic composition. [24] The glass dish is then transferred to a hot plate (Corning PC-6200), heated to 450°C (confirmed via Cen-Tech Infrared Thermometer, Item 60725) for approximately 2 h, and air cooled to room temperature for approximately 30 min. The solidified eutectic is then ground into a powder via mortar and pestle and loaded into the HOT printhead, which consists of a heated ink reservoir and custom-designed graphite nozzle. Polymer and metal alloy inks are prepared by cutting as-received poly(lactic acid) (PLA) filament (MakerBot) and Bi-Sn (American Elements®, BI-SN01-P.42SN) with metal shears to produce small pellets that fit into the HOT printhead. The sugar ink is used as-received (Isomalt, Amazon).

HOT-DIW System: The HOT-DIW system is comprised of a HOT printhead mounted to a 3D gantry stage, which moves the printhead relative to a stationary glass substrate (VWR, 2950) that is placed on a hot plate (Fisher Isotmp®, 11-800-49SHP). The HOT printhead is comprised of a nozzle contained in steel barrel that is wrapped with a heater coil (FM Keefe Company Inc., 62H36A5X-1128). This assembly is contained within a ceramic sleeve for thermal insulation and inserted into a custom mount that fixes the HOT printhead to the gantry stage. For temperature feedback, a K-type thermocouple is mounted to the HOT printhead assembly with physical contact maintained between the thermocouple bead and the HOT nozzle tip. A CMOS color camera (UI-3590CP-HQ) with 3.44 magnification is also mounted to the gantry for registering the HOT printhead at its starting position. The temperature of the HOT printhead is achieved via temperature controller (Omega®, CNi16). Typical HOT-DIW experiments are conducted by placing a glass substrate (pre-cleaned by rinsing with acetone and drying with house air and then by rinsing with ethanol and drying with house air; each step is repeated three times) onto a base plate (held at room temperature) with Kapton® tape, loading the ink into the HOT printhead (approximately 1.0 g per experiment), moving the HOT printhead to its starting position, and setting the HOT printhead to the desired nozzle temperature. Once the HOT printhead reaches a steady-state value, it is pressurized and the meanderline patterns are printed at prescribed speeds. For the AgCl-KCl eutectic system, the molten ink is heated to 400°C and printed at varying speeds at an applied pressure $P_{applied} \approx 0.44 \text{ psi}$ (3.03 kPa) through a graphite nozzle (outer diameter = 2 mm, inner diameter $\sim 200 \, \mu m$, see **Figure S8**). The printed line width is 2 mm for all speeds. The estimated flow rate for these experiments is $\sim 14~\mu L \cdot min^{-1}$. To demonstrate the broader applicability of HOT DIW, we also printed molten poly (lactic acid), PLA, a metallic alloy composed of bismuth-tin (Bi-Sn), and a carbohydrate glass composed of molten sugar through stainless steel nozzles (Tecdia Inc.) heated to 200°C onto glass substrates held at room temperature. These PLA, Bi-SN, and sugar inks are printed at

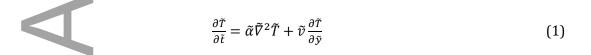


speeds of 5, 10, and 5 mm·s⁻¹ under applied pressures (Nordson EFD) of 80 psi, 20 psi, and 10 psi, respectively.



Capillary and Péclet Numbers: The relative importance of viscous and surface forces during HOT DIW of molten eutectic AgCl-KCl inks is determined by the capillary number, $Ca = \mu v/\sigma$; where μ is the viscosity of the molten ink (3.1 mPa·s), v is the print speed ($v_{max} = 4 \text{ mm·s·}^{-1}$), and σ is surface tension (145 mN·m⁻¹). Based on these values, we calculate an upper bound of $Ca_{max} = 1.2 \times 10^{-4}$. During printing, the molten eutectic wicks up the HOT nozzle thereby increasing the thickness of the as-deposited ink from $\sim 10 \, \mu m$ (gap height) to $\sim 200 \, \mu m$ before solidification (see **Movie 1**). Molten ink flow ($\sigma \approx 145 \text{ mN} \cdot \text{m}^{-1}$) minimizes energy at the top (free) surface, as the boundary changes from a constrained to free surface. This transition induces a disturbance in the form of waves (refs. [26, 27]) that solidify as the molten ink cools leaving behind sinusoidally shaped grain boundaries (defects) between lamellae (Figure S2a iii). At the substrate surface, this phenonemon is dampened leading to defect-free lamellae (Figure S2b iii). These features can also be seen in the polished cross-section of a representative printed filament (Figure S5). The curvature of the top surface of the filament arises due to surface area minimization during the printing process. A detailed view at the center of the filament (Figure S5b) reveals wavy lamellae similar to that of the top surface (Figure S2a iii), showing that the waves propagate through the filament. However, only straight lamel are observed within $\sim 2 \, \mu m$ of the bottom surface (Figure S5c). Since the ink does not readily wet the glass substrate, the width of the printed filaments is defined by the outer diameter of the nozzle. The Laplace pressure at the nozzle orifice (radius $R \approx 100 \, \mu \text{m}$) can be approximated by $\sigma/R \approx 0.7$ kPa, which is much less than $P_{applied}$. We used a small gap height of 10 μ m, i.e., below $\sigma/P_{applied} \approx 50 \,\mu$ m, to prevent the molten eutectic ink from spreading uncontrollably. We determine the Péclet number, $P_e = vT/\alpha_L$, where T is the filament thickness and α_L is the thermal diffusivity of the liquid eutectic, based on the velocity of the nozzle rather than the velocity of fluid flow. Hence, we consider the fluid motion in the reference frame of the nozzle that is translating at the printing speed, which provides the ratio between diffusive and advective heat transfer in this moving frame of reference. Using $v = v_{crit} \approx 1.0 \text{ mm} \cdot \text{s}^{-1}$, $T \approx 0.2 \text{ mm}$ (the average thickness of a typical filament, see **Figure S5a**), and $\alpha_L = 2.36 \times 10^{-1} \text{ mm}^2 \cdot \text{s}^{-1}$ (see **Table S1**) yields $P_e \approx 0.85$ at v_{crit} .

Heat Transfer Calculations: The steady-state temperature profile of the center of the filament is simulated by solving an equation that accounts for the thermal diffusion and the velocity due to the moving frame of reference, which follows the motion of the nozzle at a printing speed \tilde{v} :





where \tilde{T} is the temperature, \tilde{t} is the time, and $\tilde{\alpha}$ is the thermal diffusivity. Tildes denote non-dimensionalized variables, which are rescaled by the length scale $W_h = 2.5 \times 10^{-5}$ m and the time scale $\tau_h = 2.5 \times 10^{-3}$ s. W_h and τ_h are on the order of α/v and α/v^2 , respectively. Temperatures are non-dimensionalized by a factor of 1 K. The x-axis is parallel to the width of the filament, the y-axis is parallel to the printing direction, and the z-axis is parallel to the thickness of the filament. The printed filament is treated as a rectangular prism, where the bottom surface $(\tilde{z}=0)$ is in contact with the substrate and is subjected to Newton's law of cooling:

$$J_{\tilde{z}=0} = \tilde{h}_{sub} (\tilde{T}_{\tilde{z}=0} - \tilde{T}_{sub}) = -\tilde{k} \frac{\partial \tilde{T}}{\partial \tilde{z}} |_{\tilde{z}=0}$$
 (2)

where J is the heat flux, \tilde{h}_{sub} is the heat transfer coefficient of the substrate, \tilde{T}_{sub} is the substrate temperature, and \tilde{k} is the thermal conductivity of the eutectic. Equation (2) is used to enforce a Neumann boundary condition at the substrate-filament interface. Neumann boundary conditions are enforced at the edges and top of the filament, replacing h_{sub} and T_{sub} with the heat transfer coefficient to air (h_{air}) and the air temperature (T_{air}) , respectively. In the y-direction, no-flux boundaries are applied at the front and back of the filament domain. A cylindrical Dirichlet boundary represents the nozzle and is set to the temperature of the nozzle (T_{nozzle}) . This cylinder is centered at the maximum y-coordinate of the filament domain and has an outside diameter of d_{noz} . The diameter of the filament is taken to be 3% greater than the nozzle diameter to account for the slight spreading of the molten ink observed during the printing process. The gap height between the nozzle exit and the substrate is 10 μ m.

Thermal properties differ between the molten and solidified AgCl-KCl eutectic material. A smoothly varying function to interpolate between liquid and solid values of the thermal diffusivity $\tilde{\alpha}$ and the thermal conductivity \tilde{k} as a function of temperature is needed for numerical convergence. The interpolation function g is given by:

$$g = \frac{3(\tilde{T} - \tilde{T}_S)^2}{(\tilde{T}_L - \tilde{T}_S)^2} - \frac{2(\tilde{T} - \tilde{T}_S)^3}{(\tilde{T}_L - \tilde{T}_S)^3}$$
(3)

where \tilde{T}_s and \tilde{T}_L are the lower and upper bounds of the temperature range used for the interpolation. For temperatures between \tilde{T}_s and \tilde{T}_L , $\tilde{\alpha}$ and \tilde{k} are given by:

$$\tilde{\alpha} = \tilde{\alpha}_{S}(1 - g) + \tilde{\alpha}_{L}g \tag{4}$$

$$\tilde{k} = \tilde{k}_s (1 - g) + \tilde{k}_L g \tag{5}$$



where $\tilde{\alpha}_s$ is the solid thermal diffusivity, $\tilde{\alpha}_L$ is the liquid thermal diffusivity, \tilde{k}_s is the solid thermal conductivity, and \tilde{k}_L is the liquid thermal conductivity. For temperatures below \tilde{T}_s , $\tilde{\alpha} = \tilde{\alpha}_s$ and $\tilde{k} = \tilde{k}_s$. For temperatures above \tilde{T}_L , $\tilde{\alpha} = \tilde{\alpha}_L$ and $\tilde{k} = \tilde{k}_L$. \tilde{T}_s and \tilde{T}_L are chosen to be 1.25 below and above the eutectic temperature, respectively. This range is minimal while still ensuring numerical convergence. A correction term is added for the latent heat rejected at the solidification front over the same temperature range as the interpolation function g. For temperatures between \tilde{T}_s and \tilde{T}_L , Eq. 1 becomes:

$$\frac{\partial \tilde{T}}{\partial \tilde{t}} = \tilde{\alpha} \tilde{V}^2 \tilde{T} + \tilde{v} \left[1 + \left(\frac{c_L}{c_s} - 1 \right) g + \left(\frac{c_L}{c_s} - 1 \right) \tilde{T} \frac{\partial g}{\partial \tilde{\tau}} + \frac{L_E}{c_s} \frac{\partial g}{\partial \tilde{\tau}} \right] \frac{\partial \tilde{T}}{\partial \tilde{y}} \tag{6}$$

where c_s and c_L are the heat capacities of the solid and liquid eutectic, respectively, and L_E is the latent heat for the eutectic mixture.

The physical constants used to parameterize the temperature profile model for AgCl-KCl are summarized in **Table S1**. The model is discretized using a centered finite difference scheme and a forward Euler time stepping scheme. For $\partial \tilde{T}/\partial \tilde{y}$ in the velocity term, an upwinding Essentially Non-Oscillatory (ENO) scheme is utilized (ref. [28]) The dimensionless grid spacing $\Delta \tilde{x}$ and time step $\Delta \tilde{t}$ are 0.05 and 2.5×10⁻⁵, respectively. The code is parallelized via domain decomposition using the message passing interface (MPI) library.

2D simulations of a vertical slice within the central region of the filament are performed under steady-state conditions to determine the solidification front orientation in the y-z plane. These 2D simulation adequately capture the behavior at the center of the filament while allowing for a large number of printing speeds to be explored without incurring a large computational cost. The solidification front orientation is calculated as the angle between the printing direction and the surface normal of the contour curve at the eutectic temperature, averaged over the thickness of the filament.

3D simulations are carried out under steady-state conditions to determine the thermal gradients in the y-direction and the orientation of the solidification front in the x-y plane at the bottom surface of the filament (see **Figure S9**). The solidification front orientation is calculated by finding the angle between a linear fit to the contour curve at the eutectic temperature (the solidification front) and the printing direction. The linear fit is applied to the outermost 1% of the filament width to find the solidification front orientation at the edge of the filament and the innermost 1% to one side of the center of the filament width to find the solidification front orientation at the center of the filament. The thermal gradients and solidification front orientations are then used to set up the phase field simulation.





Lamellar Growth Model: Solidification of the AgCl-KCl filaments is simulated using a phase field model developed by Folch and Plapp (ref. [29]). The phase of each point in the simulated system is described by three non-conserved order parameters (p_{AgCl} , p_{KCl} , p_{L}), which are constrained at each point such that $p_{AgCl} + p_{KCl} + p_{L} = 1$. The order parameters take values of $p_{AgCl} = 1$, $p_{KCl} = 0$, $p_{L} = 0$ in the solid AgCl phase; $p_{AgCl} = 0$, $p_{KCl} = 1$, $p_{L} = 0$ in the solid KCl phase; and $p_{AgCl} = 0$, $p_{KCl} = 0$, $p_{L} = 1$ in the liquid phase (molten AgCl-KCl). The interfaces between phases have order parameter values that vary smoothly between zero and one. The evolution of each order parameter p_i , where the subscript i indicates the AgCl, KCl, or liquid phase, is described by the Allen-Cahn equation:

$$\tilde{\tau}(\vec{p})\frac{\partial p_{i}}{\partial \tilde{t}} = \tilde{V}^{2}p_{i} + \frac{2}{3} \left[-2p_{i}(1-p_{i})(1-2p_{i}) + \sum_{j\neq i} p_{j}(1-p_{j})(1-2p_{j}) \right] + \tilde{\lambda} \sum_{j} \frac{\partial g_{j}}{\partial p_{i}} \Big|_{p_{AgCl} + p_{KCl} + p_{L} = 1} \left(\mu A_{j} - B_{j} \right)$$

$$(7)$$

where all interfacial energies between the three phases are assumed to be equal. Here, $\tilde{\tau}$ is the relaxation time, \tilde{t} is the simulation (dimensionless) time, $\tilde{\lambda}$ is a coupling constant, g_i is a tilting function which raises the energy well of phase i, and A_i and B_i are the equilibrium concentration and equilibrium chemical free energy for phase i, respectively. Tildes again indicate dimensionless variables. The derivation of this Allen-Cahn equation is described in detail in ref. [29].

The evolution of the chemical composition at each point in the system is calculated using the diffusion equation. Writing the diffusion equation in terms of the chemical potential and including an antitrapping current explained in ref. [29] gives:

$$\frac{\partial \mu}{\partial \tilde{t}} = \tilde{V} \cdot \left(\tilde{D} p_L \tilde{V} \mu \right) - \sum_{i=AgCl,KCl} A_i \frac{\partial p_i}{\partial \tilde{t}} + 2a \sum_{i=\alpha,\beta} (A_i - A_L) (-\hat{n}_L \cdot \hat{n}_i) \tilde{V} \cdot \left(\hat{n}_i \frac{\partial p_i}{\partial \tilde{t}} \right)$$
(8)

where \widetilde{D} is the diffusion coefficient, $a=1/(2\sqrt{2})$, and \widehat{n}_i is the unit vector normal to the interface of phase i. The scaled dimensionless equilibrium concentration of phase i is defined as $c_i=(C_i-C_E)/\Delta C$ where C_i is the molar fraction KCl equilibrium concentration of phase i, C_E is the eutectic point concentration, and ΔC is the difference in the equilibrium concentrations of the two solid phases (in this case, $\Delta C=1$).

Phase transformations in the phase field model are driven by changes in the free energy landscape with changing temperature. The terms that define the temperature dependence of the



free energy curves (A_i and B_i) vary from those described in ref. [29], because of the lack of any solubility of KCl in the AgCl solid phase and vice versa. A_i and B_i and are defined as:

$$A_{i} = c_{i} - \frac{(\tilde{y} - \tilde{v}\tilde{t} - \tilde{y}_{int}(x))\tilde{G}}{m_{i}\Delta C}$$

$$B_{i} = A_{i} \frac{(\tilde{y} - \tilde{v}\tilde{t} - \tilde{y}_{int}(x))\tilde{G}}{m_{i}\Delta C}$$

$$(9)$$

The x- and y-directions are the same as those defined in the temperature profile model, \tilde{v} is the printing velocity, and \tilde{G} is the thermal gradient along the y-direction, and m_i is the liquidus slope for phase i. $\tilde{y}_{int}(x)$ is the initial position in the y-direction of the eutectic temperature isotherm as a function of x. $\tilde{y}_{int}(x)$ is based on the shape of the solidification front calculated by the temperature profile model. Since only the relative difference between A_i and A_L is relevant, we set $A_L = 0$ and $B_L = 0$.

The physical constants used to parameterize the model for the AgCl-KCl system are provided in **Table S1**. Note, that the thermal gradient for simulations of the edge of the filament use a thermal gradient that is higher than that calculated by the temperature profile method $(1.5\times10^7~{\rm K~m^{-1}})$ to encourage nucleation of new lamellae. A higher thermal gradient is expected because the experiment shows a curved surface in which the filament edge becomes thin, a feature not captured in the temperature profile model. A centered finite difference scheme with forward Euler time stepping is used to discretize the model. Variables are non-dimensionalized using the length scale W_p and time scale τ_p . W_p is chosen such that the ratio between the expected lamellar spacing and W_p is at least 64; τ_p is the average of the relaxation times of the AgCl and KCl phases as described in ref. [29]. The current phase field model does not account for the differences in molar volume between AgCl and KCl. Therefore, the volume fraction of the simulated microstructure takes the same value as the molar fraction (70% AgCl/30% KCl), rather than the actual volume fraction (62% AgCl/38% KCl). However, we do not believe that the morphology is significantly affected by this discrepancy because of the system's tendency to form lamellar features.

For the center of the filament, $W_p = 5.0625 \times 10^{-9}$ m and $\tau_p = 3.78 \times 10^{-8}$ s. For the edge of the filament, $W_p = 1.0125 \times 10^{-8}$ m and $\tau_p = 3.03 \times 10^{-7}$ s. Greater values of W_p and τ_p are used for the edge of the filament, because the lamellar feature size is larger. The dimensionless grid spacing $\Delta \tilde{x}$ is 0.8 and the time step $\Delta \tilde{t}$ is 2.29×10^{-2} for the center and 1.15×10^{-2} for the edge. Simulations of the center of the filament use periodic boundary conditions in the x-direction because the isotherm is parallel with the x-axis; while simulations of the edge of the filament used no-flux boundaries in the x-direction. In both cases, no-flux boundaries are used in the y-direction. The code is parallelized by way of domain decomposition using the message passing interface (MPI) library.



An initial set of AgCl-KCl lamellae with a small periodicity of 32.4 nm (on the order of one tenth of the experimentally observed spacing) is used to allow lamellar merging so that a natural lamellar spacing evolves at steady state. The initial lamellar spacing is perturbed by 5%. The initial lamellar pairs have spacings varying randomly by 5% to break the symmetry of the initial conditions and allow for a less constrained evolution. The initial solidification front is set to have the same orientation as eutectic temperature isotherm with some initial estimate for the undercooling (set by the distance in the y-direction between the solidification front and eutectic isotherm). The initial concentration of the liquid is uniformly at the eutectic concentration. The simulation domain shifts to follow the solidification, discarding the coldest row of gridpoints in the solid and adding a row to the hottest part of the liquid each time the solidification front progresses by one gridpoint in the y-direction. The simulations are continued until a stable microstructure is observed.



Printed Filament Microstructures: High magnification images of the printed AgCl-KCl eutectic filaments are obtained using a Zeiss Ultra Plus Field Emission scanning electron microscope (FESEM). The procedure to determine L and φ is as follows. First, the images are captured so that the print direction of the filaments is aligned with the vertical edge of the SEM field of view. Next, SEM images are acquired in the middle and side of the filament at appropriate magnifications for distinguishing separate phases of the lamellae. Image analysis is carried out using an in-house MATLAB script based on a 2D fast Fourier transform in the spatial domain to determine the average L and φ for each image. Eutectic composition and KCl phase etching are confirmed via Energy-dispersive X-ray spectroscopy (EDS) (Zeiss Supra55VP FESEM) (see Figures S10 and S11, respectively). The large field of view SEM featured in Figure 2a is obtained by mounting the sample to an aluminum pin mount using conductive carbon tape and imaging with a Tescan Vega3 GMU SEM.

KCl Phase Etching and Replacement: To etch the KCl phase, the printed filaments are immersed into an ethanol bath for 30 min. The etched filaments are then removed from the bath and air dried with a light stream of house air. The resulting etch depth is ~2.5 μ m (**Figure S12**). If desired, a silver (Ag) coating is then deposited using electron beam evaporation at a rate of 3 Å·s⁻¹ at a pressure of 1 \times 10⁻⁶ Torr. A fast rate of deposition is used to minimize localized island formation in the Ag film growth process. No adhesion layer is used in this process to avoid affecting the optical properties of the device.

Optical Measurements: Grating efficiency measurements are obtained using a light source, which consists of a fiber-coupled tunable laser (SuperK Varia). The beam is collimated by a fiber-coupled collimator (Thorlabs RC12APC-P01) with a beam size diameter of 1 cm and passed through a Glan-Thompson polarizer (Thorlabs GTH10). The collimated beam is focused



on the sample with a plano-convex lens with focal length of 15 cm resulting in a Gaussian beam with full width at half maximum of 100 µm. The optical power of the diffracted beam is measured in reflection mode by an optical power meter. The input wavelength is swept from 480 nm to 700 nm and accordingly the optical power meter position is adjusted to measure the diffraction efficiency of the grating (due to change in the grating diffraction angle with wavelength). Diffraction efficiency is defined as the ratio of optical power of the diffracted beam to that of the incident beam. Grating angular distributions are measured as follows. We mount a multimode fiber paired with a spectrometer (OceanOptics USB4000 UV-VIS) on a rotation stage to measure the angular distribution of far-field reflection from the grating under broadband illumination. The rotation stage is moved by steps of 0.2° to collect the diffracted beam by the fiber and send it to the spectrometer. The method for measuring the local spectra reflected by the top of the filaments is as follows. The local spectra are measured by putting a multi-mode fiber (600 µm diameter), which connects to a spectrometer (Ocean USB4000), at the image plane of a Zeiss microscope system (Discovery V20 with an AxioCam ERc 5s camera and a CL 1500 ECO light source). The use of the multi-mode fiber can filter the unwanted background allowing us to measure the spectrum of $\sim 175 \times 175 \,\mu\text{m}^2$ area of a sample. The measured spectra are normalized to a reference signal obtained by replacing our sample with an aluminum mirror.

Optical Simulations: The diffraction spectra and absolute efficiencies are calculated using a finite-difference time-domain (FDTD) simulation (using the commercial software from Lumerical, Inc.). The refractive index data of AgCl and KCl[30-32] are fitted with the multicoefficient model (6 coefficients) in the wavelength range 400-800 nm setting the imaginary components as 0. The refractive indices for Ag are taken from the experimental results of Johnson and Christy.[33] The calculations for the reflection diffraction grating are done on an ideal lamellar structure, applying periodic boundary conditions, with its lamellar period as obtained from the SEM analysis of the as-printed eutectic AgCl-KCl filaments. For the etched filaments, KCl is replaced by air, and for the Ag-coated case, a uniformly thick layer of Ag is placed on top of the AgCl layer. Perfectly matched layer (PML) absorbing boundary conditions were applied in the direction of propagation, and the physical structure (2µm thick) was extended up to this PML boundary. Simulations were performed for normal incident plane waves polarized perpendicularly to the grating period, and far-field projection was used from the reflection monitors. The angle dependent far-field projections were obtained using highresolution top-hat illumination, taking 20 periods. The far-field projection data of the diffraction grating was normalized to the highest intensity within the 1st and 2nd order regime.





Supporting Information

Supporting Information is available from the Wiley Online Library or from the author.



This material is based upon work supported by the Air Force Office of Scientific Research MURI FA9550-12-0471. A. K. would like to thank Daniel Bacon-Brown for discussions and help with the FDTD simulations. E. H. and K. T. acknowledge the computational resources from the DoD High Performance Modernization Program and from the University of Michigan's Advanced Research Computing. We would also thank Dr. J. Weaver for SEM assistance and Dr. L. Sanders for assistance with photography and videography. J.A.L. gratefully acknowledges support from the Vannevar Bush National Security Science and Engineering Faculty Fellowship (ONR Award No. N00014-16-1-2823).





References

- [1] H. A. Atwater, Scientific American 2007, 296, 56.
- [2] C. M. Lieber, MRS Bulletin 2003, 28, 486.
- [3] D. Schurig, J. J. Mock, B. J. Justice, S. A. Cummer, J. B. Pendry, A. F. Starr, D. R. Smith, Science 2006, 314, 977.
- [4] J. Valentine, J. Li, T. Zentgraf, G. Bartal, X. Zhang, Nat Mater 2009, 8, 568.
- [5] M. Selvanayagam, G. V. Eleftheriades, Physical Review X 2013, 3, 041011.
- [6] X. Ni, Z. J. Wong, M. Mrejen, Y. Wang, X. Zhang, Science 2015, 349, 1310.
- [7] N. Engheta, Science 2007, 317, 1698.
- [8] N. Yu, P. Genevet, M. A. Kats, F. Aieta, J.-P. Tetienne, F. Capasso, Z. Gaburro, Science 2011, 334, 333.
- [9] X. Ni, N. K. Emani, A. V. Kildishev, A. Boltasseva, V. M. Shalaev, Science 2012, 335, 427.
- [10] D. L. Sounas, C. Caloz, A. Alù, Nature Communications 2013, 4.
- [11] A. Silva, F. Monticone, G. Castaldi, V. Galdi, A. Alù, N. Engheta, Science 2014, 343, 160.
- [12] S. H. Kang, M. D. Dickey, MRS Bulletin 2016, 41, 93.
- [13] M. N. Croker, R. S. Fidler, R. W. Smith, Proceedings of the Royal Society of London A: Mathematical, Physical and Engineering Sciences 1973, 335, 15.
- [14] J. Kim, L. K. Aagesen, J. H. Choi, J. Choi, H. S. Kim, J. Liu, C.-R. Cho, J. G. Kang, A. Ramazani, K. Thornton, P. V. Braun, Advanced Materials 2015, 27, 4551.
- [15] M. Massaouti, A. A. Basharin, M. Kafesaki, M. F. Acosta, R. I. Merino, V. M. Orera, E. N. Economou, C. M. Soukoulis, S. Tzortzakis, Opt. Lett. 2013, 38, 1140.
- [16] R. I. Merino, M. F. Acosta, V. M. Orera, Journal of the European Ceramic Society 2014, 34, 2061.
- [17] D. A. Pawlak, K. Kolodziejak, S. Turczynski, J. Kisielewski, K. Rożniatowski, R. Diduszko, M. Kaczkan, M. Malinowski, Chemistry of Materials 2006, 18, 2450.
- [18] D. A. Pawlak, S. Turczynski, M. Gajc, K. Kolodziejak, R. Diduszko, K. Rozniatowski, J. Smalc, I. Vendik, Advanced Functional Materials 2010, 20, 1116.
- [19] K. Sadecka, M. Gajc, K. Orlinski, H. B. Surma, A. Klos, I. Jozwik-Biala, K. Sobczak, P. Dluzewski, J. Toudert, D. A. Pawlak, Advanced Optical Materials 2015, 3, 381.



- [20] K. Sadecka, J. Toudert, H. B. Surma, D. A. Pawlak, Opt. Express 2015, 23, 19098.
- [21] J. D. Hunt, K. A. Jackson, Transactions of the Metallurgical Society of Aime 1966, 236, 843.
- [22] K. A. Jackson, J. D. Hunt, Transactions of the Metallurgical Society of Aime 1966, 236, 1129.
- [23] J. D. Hunt, K. A. Jackson, Transactions of the Metallurgical Society of Aime 1967, 239, 864.
- [24] E. Fischer, Journal of Phase Equilibria 2003, 24, 228.
- [25] G. J. Janz, R. P. T. Tomkins, C. B. Allen, J. R. Downey, G. L. Garner, U. Krebs, S. K. Singer, Journal of Physical and Chemical Reference Data 1975, 4, 871.
- [26] E. Jens, V. Emmanuel, Reports on Progress in Physics 2008, 71, 036601.
- [27] L. Rayleigh, Proceedings of the London Mathematical Society 1878, s1-10, 4.
- [28] S. Osher, *Level Set Methods and Dynamic Implicit Surfaces*, Springer New York, 2003.
- [29] R. Folch, M. Plapp, Physical Review E 2005, 72, 011602.
- [30] L. W. Tilton, E. K. Plyler, R. E. Stephens, J. Opt. Soc. Am. 1950, 40, 540.
- [31] H. H. Li, Journal of Physical and Chemical Reference Data 1976, 5, 329.
- [32] M. N. Polyanskiy, "Refractive index database", http://refractiveindex.info (accessed March 5 2016).
- [33] P. B. Johnson, R. W. Christy, Physical Review B 1972, 6, 4370.

Figure 1. HOT-DIW of molten eutectic inks. (a) Overview of printing system and list of components (main) with photograph of system (inset). (b) Detail side view schematic of printing process showing the solidification front following the HOT nozzle. Figure is drawn to scale to match the physical process. The nozzle inner diameter is $\sim 200 \ \mu m$. (c) Micro-scale schematic of solidification front showing solid-liquid interface and the lamellar growth during the printing process. In this case, the dark lamellae (α-phase) represent KCl and the light gray lamellae (β-phase) represent AgCl. J_A and J_B represent the flux of KCl and AgCl, respectively, into their corresponding solid phases.



Figure 2. Printed eutectic AgCl-KCl filaments. (a) Macro-scale SEM image of typical printed meander pattern. (b) Representative images of printed filament (bottom surface), including (i) low magnification and (ii-iii) high magnification views along with (iv-v) corresponding predicted images from phase field modeling of filament edge (blue) and center (red), respectively. The experimental data and simulations correspond to $v = 0.18 \, \mathrm{mm \cdot s^{-1}}$.

Figure 3. Controlling lamellar spacing in printed eutectic AgCl-KCl filaments. (a) SEM images of eutectic filaments (center region, bottom surface) printed at speeds below and above v_{crit} . [Note: Arrow shown in the image at $v=1.14~\rm mm\cdot s^{-1}$ denotes the formation of a domain boundary within the printed filament.] Scale bars are 2 µm. (b) 2D heat transfer simulations of the central region of printed filaments as a function of printing speed, which reveal the temperature fields (left column) and resulting solidification fronts (right column). The HOT nozzle interface is located at position 4214 µm in the print direction. (c) Lamellar spacing measured within the printed filaments as a function of print speed. White region denotes filaments printed below v_{crit} , where lamellae of uniform orientation are observed. Gray region denotes filaments printed above v_{crit} , which contain lamellae that are non-uniform in orientation. (d) Lamellar spacing as a function of solidification front velocity.

Figure 4. Optical properties of printed, etched, and coated filaments. (a) Optical image of diffraction patterns of a broadband light source reflecting off of the bottom surface of a printed eutectic AgCl-KCl filament (main) [Inset shows schematic view of procedure used to measure spectra and efficiency of reflected light.] (b) Representative (top) measured and (bottom) simulated spectra of reflected light for a eutectic filament printed at $v = 0.01 \, \mathrm{mm \cdot s^{-1}}$ ($L \approx 1749 \, \mathrm{nm}$). (c) (top) Measured and (bottom) simulated normalized diffraction efficiency of first order for wavelength at center of visible spectrum ($\lambda = 515 \, \mathrm{nm}$) for eutectic filaments printed at $v = 0.01 \, \mathrm{mm \cdot s^{-1}}$ ($L \approx 1749 \, \mathrm{nm}$) (black), $v = 0.05 \, \mathrm{mm \cdot s^{-1}}$ ($L \approx 801 \, \mathrm{nm}$) (red), and $v = 0.1 \, \mathrm{mm \cdot s^{-1}}$ ($L \approx 606 \, \mathrm{nm}$) (blue). (d) Measured absolute diffraction efficiency for as-printed ($v = 0.05 \, \mathrm{mm \cdot s^{-1}}$), KCl-etched, and KCl-etched and coated with silver (450 nm thick), where $L \approx 801 \, \mathrm{nm}$.





TOC caption:

High operating temperature direct ink writing (HOT-DIW) of mesoscale eutectic architectures composed of AgCl-KCl. The molten ink undergoes directional solidification upon printing on a cold substrate. The lamellar spacing of the printed features can be varied between $\sim\!100$ nm-2 μ m, enabling the manipulation of light in the visible and infrared range.